Short-Range Non-Bending Fully Distributed Water/Humidity Sensors

George Y. Chen ⬤, Xuan Wu, Erik P. Schartner ⬤, Soroush Shahnia ⬤, Nicolas Bourbeau Hébert ⬤, Li Yu,
Xiaokong Liu, Shahraam Afshar V., Trevor P. Newson, Heike Ebendorff-Heidepriem ⬤, Haolan Xu ⬤,
David G. Lancaster ⬤, and Tanya M. Monro ⬤

Abstract—**Existing sensing technologies lack the ability to spatially resolve multiple sources of water or humidity without relying on the deployment of numerous inline sensors. A fully distributed approach has the potential to unlock a diverse range of applications, such as humidity mapping and liquid-depth measurements. We have explored a new direction toward what is, to the best of our knowledge, the first non-bending fully distributed water/humidity sensors. This new class of sensors was made possible from the first combination of small-core exposed-core fiber, a hydrophilic polyelectrolyte multilayer coating, and coherent optical frequency-domain reflectometry. Their non-bending nature enables deployment in a wider range of environments compared to the bending type based on water-induced fiber bending. The sensing mechanism involves monitoring back-reflected optical signals created by changes in the local reflectivity due to water-induced reduction in the local refractive-index of the coating. The demonstrated average sensitivity of the sensing fiber with 10.0 bilayer polyelectrolyte multilayer coating to relative humidity varies from 0.060 to 0.001 /%RH (0–38 cm distance) within a dynamic range of 26–95%RH. The distance-dependent detection limit varies between 0.3–10.0%RH (0–38 cm distance), and the spatial resolution of 4.6 mm is the smallest demonstrated for exposed-core fibers and can be vastly improved by simply broadening the swept range. The response time is 4–6 s, and the recovery time is 3–5 s. The sensing range (i.e., distance) is −0.5 m, which is more suitable for water-depth monitoring.**

Index Terms—**Distributed, exposed core, frequency, humidity, hygrometer, OFDR, optical fiber, polyelectrolyte coating, reflectometry, sensor, water.**

G. Y. Chen, S. Shahnia, S. Afshar V., D. G. Lancaster, and T. M. Monro are with the Laser Physics and Photonic Devices Laboratories, School of Engineering, University of South Australia, Adelaide, SA 5095, Australia (e-mail: george.chen@unisa.edu.au; soroush.shahnia@unisa.edu.au; Shahraam.AfsharVahid@unisa.edu.au; david.lancaster@unisa.edu.au; tanya.monro@unisa.edu.au).

X. Wu and H. Xu are with the Future Industries Institute, University of South Australia, Adelaide, SA 5095, Australia (e-mail: xuan.wu@unisa.edu.au; haolan.xu@unisa.edu.au).

E. P. Schartner is with the Institute for Photonics and Advanced Sensing and School of Physical Sciences, University of Adelaide, Adelaide, SA 5005, Australia, and also with the ARC Centre of Excellence for Nanoscale BioPhotonics, Adelaide, SA 5005, Australia (e-mail: erik.schartner@adelaide.edu.au).

T. P. Newson is with the Optoelectronics Research Centre, University of Southampton, Southampton SO17 1BJ, U.K. (e-mail: tpn@soton.ac.uk).

N. Bourbeau Hébert is with the Centre d'optique, photonique et laser, Université Laval, Québec, QC G1V 0A6, Canada (e-mail: nicolas.bourbeau-hebert.1@ulaval.ca).

L. Yu is with the Shenzhen Key Laboratory of Laser Engineering, Key Laboratory of Optoelectronic Devices and Systems of Ministry of Education and Guangdong Province, College of Optoelectronic Engineering, Shenzhen University, Shenzhen 518060, China (e-mail: li.yu@szu.edu.cn).

X. Liu is with the State Key Laboratory of Supramolecular Structure and Materials, Collage of Chemistry, Jilin University, Changchun 130012, China (e-mail: xiaokongliu@jlu.edu.cn).

H. Ebendorff-Heidepriem is with the Institute for Photonics and Advanced Sensing and School of Physical Sciences, University of Adelaide, Adelaide, SA 5005, Australia (e-mail: heike.ebendorff@adelaide.edu.au).

Color versions of one or more of the figures in this paper are available online at http://ieeexplore.ieee.org.

Digital Object Identifier 10.1109/JLT.2019.2897346

I. Introduction

WATER connects every aspect of life, and it is a precious resource to all of us. The world is currently facing a global water crisis. There are 844 million people living without access to safe water [1], and 1 million deaths per year due to water, sanitation and hygiene-related diseases. Hence, the ability to monitor the depth of water or the distribution of relative humidity (RH) in soil is essential for careful management of sustainable water usage for agriculture and forestry. Overcoming this hurdle and using ground RH data from satellite imaging could for the first time, provide a real-time 3-dimensional map of underground water, which can enable smarter usage of water by the agriculture and forestry industries to save significant costs.

Although there are technologies for measuring RH with multiple point sensors or quasi-distributed sensors [2], [3], the cost is proportional to the number of sensing points, which can be expensive for large-area or high spatial-resolution coverage. Fully distributed sensors could be a key technology to address these challenges with its value for money. Such sensors [4]–[8] relying on various types of reflectometry are amongst the most commercially successful optical fiber-based sensors, alongside fiber Bragg gratings [9], fiber-optic gyroscopes [10] and other single-mode/multimode fiber-based sensors [11], [12]. It is well known that fiber-optic sensors are immune to electromagnetic interference [13], and are widely used to monitor spatially resolved temperature [5], strain [6], pressure [7] and vibrations [8] for structural-health monitoring of buildings, mines and oilrigs.

To date, there is a lack of non-bending fully distributed water/humidity sensors. Progress has been made as far as

interrogating a finite number of sensing points with optical time-domain reflectometry (OTDR) [3], which relies on water-induced absorption of light. However, it is a quasi-distributed sensor (20–80%RH dynamic range, 2%RH detection limit/accuracy, 1 s time constant, 20 m spatial resolution), and it was not possible to expand the sensing point to cover the entire length of the optical fiber as a fully distributed sensor due to several reasons. Firstly, the humidity-sensitive coatings known at the time have higher refractive-indices (RIs) than that of the core, which can rapidly attenuate the optical signal and restricts the sensing range. Secondly, there were no practical optical fibers with a continuously exposed yet protected core (i.e., narrow passage for water-vapor transfer but blocks large/viscous contaminants) that offers single-mode guidance, which is required for effective use of the OTDR technique. Another demonstration was made using a hydrogel-coated optical fiber interrogated with OTDR [14], which relies on water-induced bend perturbations. Although this is a fully distributed sensor, the reliance on mechanical deformation is not suitable for uncontrolled environments due to the high likelihood of false signals generated by temperature or pressure changes in the ambient environment, as well as bending restrictions when attached to a structure such as a water pipe or wall cavity.

To address the problems of spatially resolvable water/RH monitoring with high cost, bulky cabling, ambient false signalling or direction ambiguity, we present short-range demonstrations towards the first all-optical non-bending fully distributed water/RH sensors, which contributes to the goal of establishing real-time monitoring systems [7], [15] for smart cities and agriculture/forestry. This is a new sensing platform enabled by the first combination of small-core exposed-core fiber (i.e., single-mode guidance), functional coating (i.e., specificity), and C-OFDR, which could realize a range of fully distributed bio/chemical sensors. The sensing fiber consists of a standard telecom single-mode fiber (SMF) spliced to a graded-index fiber (GIF), spliced to an exposed-core fiber (ECF) [16]. The ECF features a continuously exposed yet protected core with a hydrophilic polyelectrolyte multilayer (PEM) coating. The PEM coating has been previously demonstrated to be extremely sensitive to RH (i.e., 305 nm wavelength shift for 0–100%RH, RI change >0.1, and thickness change up to 56%) [17] and exhibits the fastest-reported response (i.e., 3 ms response time) [18]. The sensing fiber is interrogated with coherent optical frequency-domain reflectometry (C-OFDR) [19]–[21]. This choice of reflectometry is based on the notion that C-OFDR systems can exhibit lower noise and wider dynamic range than their incoherent counterparts [19]–[21]. In addition, they can offer higher spatial-resolution compared to other reflectometry techniques. Most importantly for this application, they can be made low cost by using an inexpensive distributed feedback laser to replace the tunable laser, which discards the high spatial-resolution that is far in excess of the requirements for monitoring the depth of water or the distribution of RH. The sensing fiber can be configured to exhibit a specificity only to water, or both water and water vapor, by selecting the right coating thickness, which avoids false signals from the ambient environment.
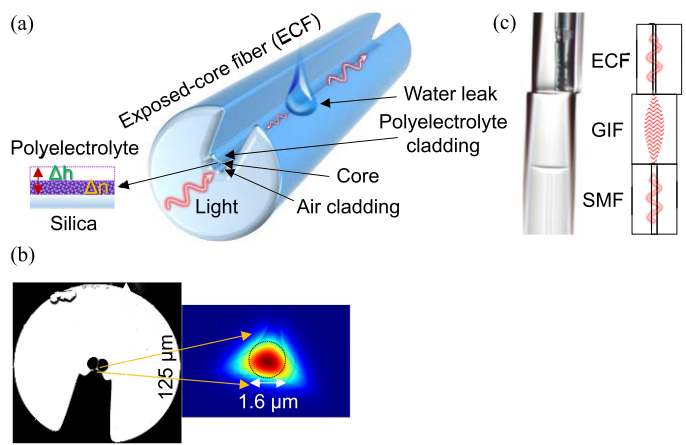

Fig. 1. (a) Illustration of the sensing fiber. Inset: cross-section view of the polyelectrolyte multilayer coating which has RI (Δn) and thickness (Δh) changes upon absorption of water. (b) (left) Scanning electron microscope image of the exposed-core fiber cross-section; (right) simulation of the mode intensity distribution in the core. (c) Construction of the sensing fiber with an exposed-core fiber (ECF), a graded-index fiber (GIF), and a single-mode fiber (SMF).

II. SENSING FIBER FABRICATION

The fabrication of the sensing fiber started with a silica ECF that features a suspended core, with a segment of silica cladding missing to allow for direct exposure of the core to the local environment. 35–40 cm sections of ECF (i.e., ~45 cm total length) shown in Figure 1(a) with a core diameter of 1.6 μm were functionalized by hydroxylation with piranha solution followed by coating 6.0, 8.0, 10.0, 12.0 or 14.0 bilayers of polyelectrolyte multilayer (PEM) coating comprising layer-by-layer-assembled poly(diallyldimethylammonium chloride) (PDDA) and poly(styrenesulfonate) (PSS) [17]. The fiber length was limited by the design of the existing dip-coating rig. The measured coating thicknesses are 800 nm (10.0 bilayers) and 1250 nm (14.0 bilayers), according to scanning electron microscope analysis. The recently reported variant of ECF [22] was chosen because its small core of 1.6 μm can achieve predominantly single-mode guidance at 1550 nm wavelength (i.e., V number is ~3, assuming 45%RH, PEM coating RI of 1.35 [17] at 1550 nm wavelength and thus cladding RI of 1.117 based on [23]), as shown in Figure 1(b). The bare cladding surrounding the suspended core improves handling by reducing the chance of oil/dirt contamination along core, eliminating one of the primary issues in the use of D-shaped fibers or nanowires [16]. Prior to coating, the bare ECF exhibited a propagation loss of ~4 dB/m at 1550 nm wavelength [22], which is comparable with that of similar optical fibers reported in the literature [24]. The propagation loss after coating will be discussed in the detection system setup section.

The response of a PEM coating to an increase in the local water/humidity is water adsorption then diffusion through their nanopores followed by swelling, resulting in a decrease in RI from ~1.4 to ~1.3, increase in coating thickness up to 56% [17], and increase in water-absorption-induced optical loss. The PDDA/PSS-based PEM coatings fabricated via layer-by-layer assembly have several qualities: (a) they are uniform in thickness

and RI across the coating [17], which leads to consistent absorption of water or water vapor to change its RI; (b) the coating enables sideways absorption parallel to the coating plane, which is useful in the case of surface contamination that blocks water across the coating surface; (c) the coating recovers its sensitivity after immersion in tap water, when tested for 1 day, which makes the coating practical; and (d) the coating exhibits insensitivity when exposed to ethanol vapor, when tested for 1 hr. Insensitivity to alcohol is due to the small-pore-sized PEM coatings being more hydrophilic and preferentially permeable for smaller polar water molecules over larger hydrophobic alcohol molecules [25]. Note, the minimum bend radius of a coated/uncoated ECF before breaking is ∼6 mm.

III. Sensing Fiber Characterization

For demonstrating the distributed water and RH sensor, a range of coating thicknesses between 6.0 and 14.0 bilayers was tested. We chose even numbers of coating layers (e.g., 10.0 bilayers) with PSS as the outmost layer, because previous studies revealed that odd numbers of coating layers (e.g., 9.5 bilayers) with PDDA as the outmost layer do not visibly affect the magnitude of the RI change to humidity [17]. Back-reflected optical signals are created by changes in the local reflectivity due to RH-induced changes in the local RI of the coating. Water-induced swelling of the PEM coating did not introduce measureable bending effects under a microscope (Nikon Eclipse LV100ND), due to the relatively small volume of the PEM coating versus the silica ECF.

In comparison, we have tested a sensing fiber based on a pristine ECF, which is hydrophobic. From 0%RH to <100%RH, the fiber surface is unresponsive. This is because the density of water vapor is not sufficient to induce a detectable RI change seen by the evanescent field of the guided light, and thus produce a measurable reflectivity change. At 100%RH or water, unresponsiveness is attributed to dispersion of water into numerous micro-droplets that scatter light along the core of the ECF, which prevents interaction with the evanescent field extended outside the core. Another comparison is a sensing fiber based on a hydroxylated ECF (i.e., with piranha solution) without a PEM coating, which is hydrophilic. From 0%RH to <100%RH, the fiber surface was found to be unresponsive, due to a small overlap between the evanescent field of light and the thin layer of adsorbed water (e.g., nanometers [26]). At 100%RH or with water, unresponsiveness is caused by water rapidly spreading and covering the entire length of the core due to its hydrophilic surface, which removes abrupt changes in RI and thus suppresses back-reflected optical signals.

The sensing fiber was spliced to a ∼190 μm length of GIF (i.e., mode-matching section) using a fusion splicer (Fujikura FSM100P), before splicing to a length of SMF (Nufern GF1) (i.e., light-delivery fiber), as shown in Figure 1(c). The sensing fiber becomes polarization maintaining after coating, due to the non-center-symmetric coating coverage. The GIF acts as a fiber lens, coupling the diverging light from the light-delivering SMF into the sensing fiber by reducing the difference between laser spot size and core diameter.
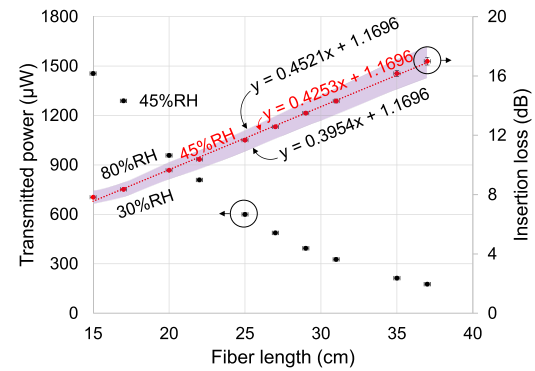

Fig. 2. Cutback measurement of the sensing fiber at different RH, plotting transmitted power and insertion loss as a function of fiber length. Black dots: transmitted power as a function of fiber length. Red dots: insertion loss as a function of fiber length. Purple shaded area: represents the range of insertion loss depending on the RH.

The coupling (i.e., into ECF) and propagation losses of the sensing fiber (i.e., along ECF) at an ambient condition of 45%RH were obtained at 1550 nm wavelength via the cutback method, as shown in Figure 2. The Fresnel reflection loss due to the gradual transition of the PEM coating along the sensing fiber is relatively weak and thus neglected. The reflection loss associated with the slight mode-coupling mismatch was neglected for the sake of simplicity. The combined Fresnel reflection losses of the flat-cleaved fiber end was approximated to be 0.10 dB with knowledge of the RI of silica (1.444 at 1550 nm wavelength [27]), the PEM coating (1.350 at 1550 nm wavelength [17]) and air (1.000 at 1550 nm). From these information, the coupling loss was calculated to be 1.07 dB, from subtracting the Fresnel reflection losses of the flat-cleaved fiber end (0.10 dB) from the insertion loss projected at a sensing fiber of zero length (1.17 dB). The propagation losses was calculated to be 0.43 dB/cm, from analyzing the gradient of the slope. The insertion losses (i.e., between SMF and photodetector) were measured with the tunable laser source set to 1550 nm wavelength, a photodetector and a power meter (Newport 919P-003-10, 843-R), with each power measurement repeated 5 times to find the errors (i.e., negligible). To provide an insight of the change in propagation loss at different RH, the transmitted power through the sensing fiber of 15 cm length was remeasured with 30%RH and 80%RH. The additional insertion loss relative to the ambient insertion-loss was divided by the fiber length to yield −0.03 dB/cm and +0.03 dB/cm respectively. Hence, the propagation loss can be as low as 0.40 dB/cm (30%RH), and as high as 0.45 dB/cm (80%RH). The inherent propagation-loss associated with coated sensing fibers is due to the Rayleigh scattering caused by the surface roughness [24] of the PEM coating at the coating-air interface (i.e., ∼100 nm root-mean-squared roughness [17], proportional to coating thickness) as well as inside the coating. For lowering the propagation loss, the fiber design can be improved in terms of optimizing the core size. The higher propagation-loss associated with higher RH is caused by water-induced absorption of light inside the PEM coating at 1550 nm wavelength [28], which is slightly counteracted by stronger optical confinement within the fiber
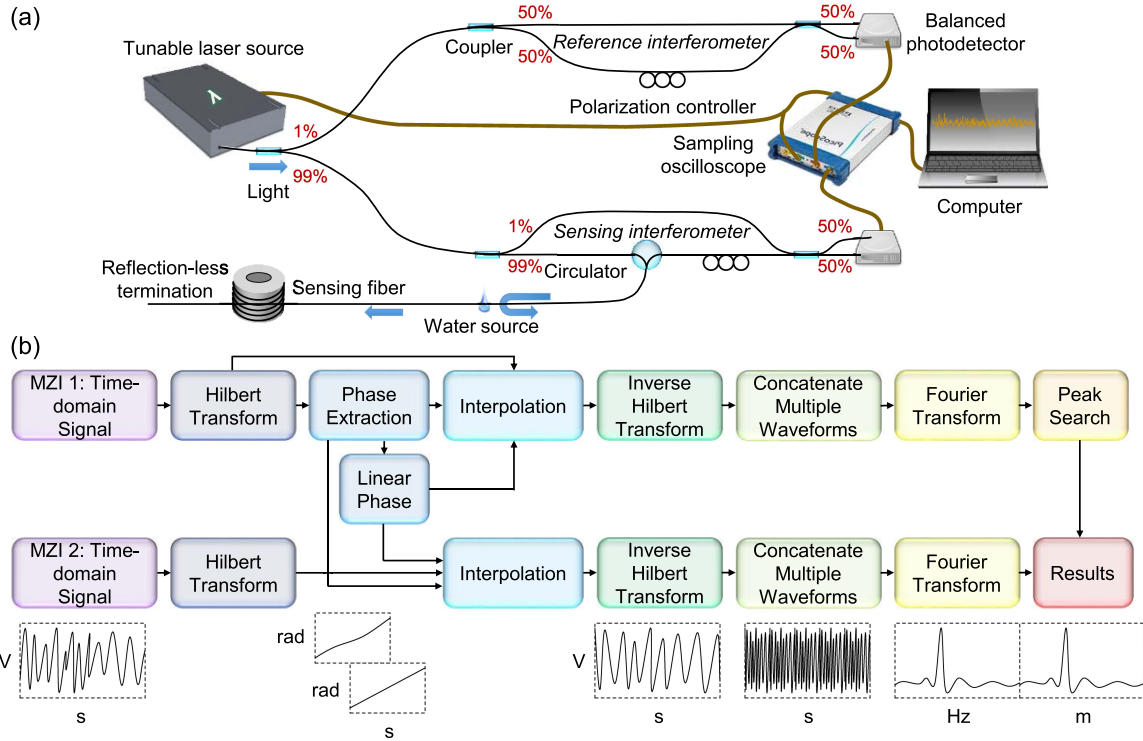
Fig. 3. (a) Schematic of the optical frequency-domain reflectometry setup. (b) Flow diagram of the signal processing performed by the computer, with illustrations of signals.

core due to the lower cladding RI. Using a wavelength that is non-water-absorbing will decrease the propagation loss for an extended sensing range. Future work will investigate the relative contribution of these two factors towards the propagation loss.

IV. DETECTION SYSTEM SETUP

As shown in Figure 3(a), the sensing fiber was incorporated in a Mach-Zehnder interferometer (MZI) via a circulator. A tunable laser source (Newspec Velocity TLB-6728-P-D, 100 Hz spectral linewidth, 187 pm continuous swept range centered at 1550 nm, 10 sweeps per second, 14.6 mW output power) launched linearly polarized light centered at 1550 nm wavelength into the SMF, before it was split into two paths via a fused coupler. The wavelength sweep was modulated ($-/+3$ V) by the built-in waveform generator of a PC oscilloscope (Picoscope 6404C). One path of light (99%) was diverted to the sensing MZI, while another path of light (1%) was diverted to a reference MZI. In the sensing MZI, a circulator regulated the return optical signals, while a polarization controller was used to maximize the interference visibility by aligning the direction of polarization to be perpendicular to the surface of the coated core for maximum penetration and interaction. The termination of the sensing fiber was simply an angle-cleaved end-face with a PEM coating. For water-depth sensing, the sensing fiber was attached to a metal pipe with tape to mimic a simple deployment method in soil. The practical challenges for field deployment include maintaining a clean sensing fiber free from dirt and contaminants that would coat the fiber. For humidity sensing, the sensing fiber was rested

above the opening of a plastic cap flushed with RH-controlled nitrogen with a ∼4 cm exposed section. The in-house RH generator [17], [18] operated by mixing dry and wet nitrogen gas. The wet nitrogen gas was generated by passing dry nitrogen gas through 70 °C and 21 °C water-filled beakers followed by a series of condensers to remove excess heat and water. The mixing ratio was regulated via two flow meters. In the reference MZI, an optical path-length difference of 7.05 m was measured. Again, a polarization controller was used for optimization. The 4 output ports of the 2 MZIs were fed into 2 balanced photodetectors (Thorlabs PDB-450C, DC to 300 kHz with 106 V/A gain), which was sampled by the PC oscilloscope with a sampling interval of 230.4 ns, 100,000 data points per sweep, and a 4-sweep first-in-first-out concatenation for running averaging. The balanced detector serves to cancel common-mode laser intensity noise and thus increase the signal-to-noise ratio, as well as to remove unwanted common-path Fabry-Perot interferences from perturbations, connections and splices. Finally, the output data was rapidly streamed and processed in real-time by a computer with no moving averages, median filter nor oversampling. To compensate for laser intensity noise and environmental instability in real-time, a self-reference technique was employed, where the amplitudes of the frequency/distance resolved spectrum of the sensing MZI were divided by the beat frequency amplitude of the dual-splice fiber region prior to the start of the sensing fiber. The upper limit of measurement refresh-rate is based on the double-pass transit time of light through the sensing fiber (i.e., to avoid frequency ambiguity), and thus it is in the order of tens of megahertz.

In terms of basic system operation, the reference MZI was used to calibrate the sensing MZI in real-time, while the tunable laser source swept the wavelength to produce interferometric signals from each perturbation along the sensing fiber. To describe in more detail, the laser wavelength was swept in a sawtooth pattern with only the rising-slope signal being triggered and the output data corresponding to the positive region being captured. The sensing fiber back-reflected light with the occurrence of perturbations along its entire length, with a cumulative sequence of wavelengths exhibiting phases proportional to the distances that the light has traveled. The reference arm of the interferometer operated using a shorter length of fiber in transmission mode. These two paths of light coherently recombined at a coupler. A single back-reflection with a specific optical path length difference relative to the reference path created a single set of interference fringes with a single beat frequency of narrow spectral linewidth ($\Delta\lambda_L$). The difference in wavelength between the two paths still allows interference, but with diminished interference visibility and a shorter coherence-length ($L_{\max}$), in addition to generating a low difference-in-frequency envelope. For multiple back-reflections, multiple sets of fringes with scaled free-spectral-ranges were superimposed, containing multiple beat frequencies. The beat frequencies correspond to the distances along the sensing fiber. The beat amplitudes are linearly proportional to the interference visibility, which is a function of the power ratio, local reflectivity, local effective RI change, local coating RI change, and thus on the local RH.

A relatively slow sweep frequency of 10 Hz was chosen to avoid beat frequency ambiguity, where back-reflected longer wavelengths from one sweep cycle (i.e., more distance traveled) beat produce a similar beat frequency to that of shorter wavelengths from the next sweep cycle in time (i.e., less distance traveled), which merges the beat frequencies with a moving averaging effect. To prevent this, the scan duration must be much longer than the double-pass transit time of light through the sensing fiber (i.e., slower measurement updates), or signal encoding must be adopted [29]. The rising slopes of the drive current were used to prevent beat frequency ambiguity, otherwise beat frequencies may overlap due to back-reflected longer wavelengths from farther distances producing similar beat frequencies to that of shorter wavelengths from nearer distances, which merges the beat frequencies with a moving averaging effect. To avert this, only rising slopes were used for the drive current. There is no beat frequency ambiguity with cavity-generated beat signals from the sensing fiber, because the balanced detector cancels them out. To achieve a monotonic relationship between RH and beat frequency amplitude, as well as to maximize the signal-to-noise ratio for a lower detection-limit, the transmitted power through the reference path of the sensing MZI must be greater or equal to the maximum transmitted power through the sensing path. The propagation loss of each path can be tailored by inducing bend loss.

Figure 3(b) gives an overview of the signal processing performed by the computer. Essentially, the raw time-domain interferometric signal was corrected, converted into the frequency domain and finally the distance domain, with the beat amplitudes being of interest. To describe in more detail, the time-

domain signals of both MZIs experienced inconsistent wavelength sweep rate of the tunable laser source. Therefore, it is required to correct these signals via time-domain resampling. Firstly, the fast Hilbert Transform was performed on the reference MZI signal (i.e., corresponding to a single wavelength sweep) to create a complex time-domain signal with phase information. The complex time-domain signal was resampled in time-domain via interpolation, involving its unwrapped phase grid, the ideal linear phase grid, and the Hilbert transformed time-domain signal. Then, the Inverse Hilbert Transform of the resampled data produced the corrected time-domain signal. After that, a succession of measurements was concatenated together for a running-average effect, before the Fast Fourier Transform (FFT) was performed to retrieve the beat frequencies. Knowledge of the sampling interval enabled the conversion from frequency bin to frequency. A peak search yielded the conversion factor from frequency to distance (i.e., 7.05 m/6850.0 Hz = 1029.2 μm/Hz), as the differential path length of the reference MZI was known. Similarly, for the sensing MZI, its time-domain signal was resampled using the phase information from the reference MZI. Then, FFT followed by frequency-distance conversion presented the frequency amplitudes as a function of distance.

The fundamental lower-limit of the spatial resolution [20] (Δz) is 4.6 mm for our system, which is determined by the swept wavelength range of the tunable laser source and can readily be improved by one order of magnitude:

$$\Delta z = \frac{\lambda^2}{2 n_{eff} \Delta\lambda_s} \tag{1}$$

where λ is the center wavelength of light (1550 nm), n_{eff} is the effective RI of the fundamental mode (1.35 from COMSOL modelling with 800 nm thick PEM coating of 1.35 RIU, 1.31 without coating), and $\Delta\lambda_s$ is the swept-wavelength bandwidth (187 pm).

However, the propagation loss of the sensing fiber sets the upper limit. With 30.0 mW of input optical power at the start of the sensing fiber, a propagation loss of 0.43 dB/cm results in a transmission of 225.0 μW after 0.5 m of propagation, from multiplying the transmitted power by the propagation loss. Assuming a local effective RI change of 0.02 (i.e., a small fraction of the >0.1 RI change observed in [17]) from the effective RI of 1.35, the local reflectivity is 5.25×10^{-5}% from Fresnel reflection. This means a back-reflected optical power of 11.8 nW from multiplying the transmitted power by the reflectivity, and a received optical power (i.e., after double pass) of 88.6 pW from multiplying the reflected power by the propagation loss, which is above the maximum measured system noise of 0.054 or 62.3 pW within the region of interest along the sensing fiber.

Although the achievable Δz is more than sufficient for mapping water/humidity, Δz can be reduced by using a tunable laser source with a broader $\Delta\lambda_s$, increasing the sweep frequency to scale up and separate the beat frequencies, and/or increasing the total sampling time to improve the frequency resolution of the Inverse Fourier Transform. We have intentionally not minimized Δz, because distributed water/humidity monitoring typically do

not require a high spatial-resolution (<1 cm). As a result, the same performance can be realized using a relatively low-cost distributed feedback laser instead, with wavelength tuning via drive-current modulation. $L_{\max}$ can be extended by lowering the propagation loss.

V. OPTICAL RESPONSE TO WATER

For sensing fibers with 6.0, 8.0 and 14.0 bilayer PEM coatings, optical responses were observed through a series of testing with a lint-free tissue soaked by tap water only when there is water (100%RH) in contact with the core of the sensing fiber. This is attributed to the sensing mechanism, where back-reflected optical signals are created by changes in the local reflectivity due to water-induced reduction in the local RI of the PEM coating. It was found that the sensing fibers with 10.0 (i.e., nominated for study) or 12.0 bilayer PEM coatings exhibited the largest responses to water.

Water interacts with the sensing fiber in unpredictable ways. The variation in the observed peak reflectivity/amplitude and the temporal characteristics are primarily attributed to the unpredictable waterfront angle relative to the fiber orientation, and the air-flow-induced unstable meniscus. Hence, the distributed water sensors can only provide a binary (i.e., water or no water) detection method. As a result, the parameters of sensitivity and detection limit are not applicable in this case.

VI. SENSITIVITY/DETECTION LIMIT OF RELATIVE HUMIDITY

Noticeable optical responses to water vapor (<100%RH) were observed only with sensing fibers paired with 10.0 (i.e., nominated for study) or 12.0 bilayer PEM coatings. The results of the sensing fiber with a 10.0 bilayer PEM coating are presented in Figure 4(a), which shows an optical response with a normalized voltage of 1.017 when exposed to a localized 95%RH. The C-OFDR was able to identify reflections from the two fiber splices, the PEM coating edge, the humidity source at a distance of 12.45 m, and the sensing fiber termination. Only the region between the coating and the sensing fiber termination is of interest, as the rest produce known artefacts.

A series of tests were carried out with an ambient 45%RH to determine the relationship between RH (26–95%) and voltage for a humidity source located at 12.5 cm along the sensing fiber, as shown in Figure 4(b). A noticeable feature is the drop in voltage around ambient RH, which is attributed to the nature of reflectometry being responsive to both negative and positive changes in RI, and will be fully explained in the discussions section. An average sensitivity of 0.020/%RH can be observed from the slopes of the linear fittings both above and below the ambient 45%RH, within the dynamic range of 26–95%RH. From the consistent sensitivities, the normalized voltages for <26%RH is anticipated to mirror that of >64%RH. The RH errors are ±1%RH according to the specifications of the commercial hygrometer. The normalized voltage errors due to system noise and measurement repeatability errors is 0.005 as shown in Figure 4(b), with the RH measurements repeated 5 times. The system noise was obtained by taking a measurement while shielding the sensing fiber from fluctuations in the ambient RH
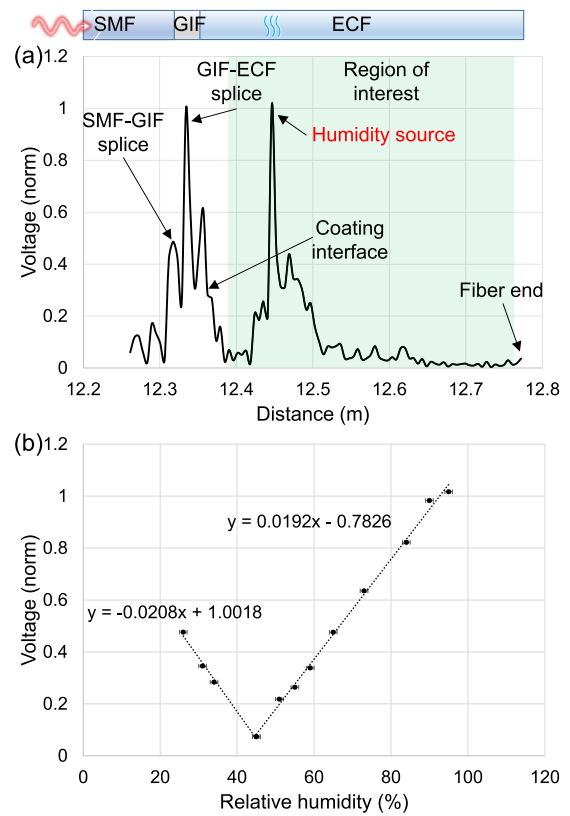

Fig. 4. (a) Spatially resolved measurement data of a sensing fiber with a 10.0 bilayer PEM coating, involving a single humidity source of 95%RH. Exposed-core fiber: ECF, graded-index fiber: GIF, and single-mode fiber: SMF. (b) Measured relationship between RH and voltage to show the sensitivities. Voltages are normalized by the highest peak of the dual-splice fiber region.
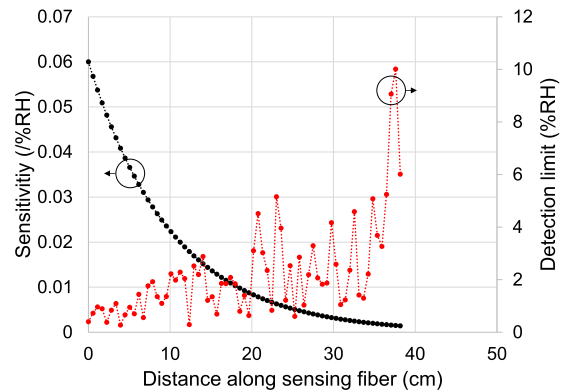

Fig. 5. Sensitivity and detection limit as a function of distance, for a sensing fiber with a 10.0 bilayer PEM coating.

with sheets of paper. A higher system noise is anticipated for a local environment with a higher RH, due to light scattering from water molecules passing in and out of the PEM coating.

The sensitivity shown in Figure 5 is projected to decline from 0.060–0.001/%RH with increasing distance (0–38 cm) along the length of the sensing fiber, with the scaling of 0.020/%RH proportional to the propagation loss (0.43 dB/cm). The distance-dependent detection limits (0.3–10.0%RH) shown in Figure 5 were deduced from dividing the distance-dependent sensitivities by the corresponding system noise (0.003–0.054, equivalent to
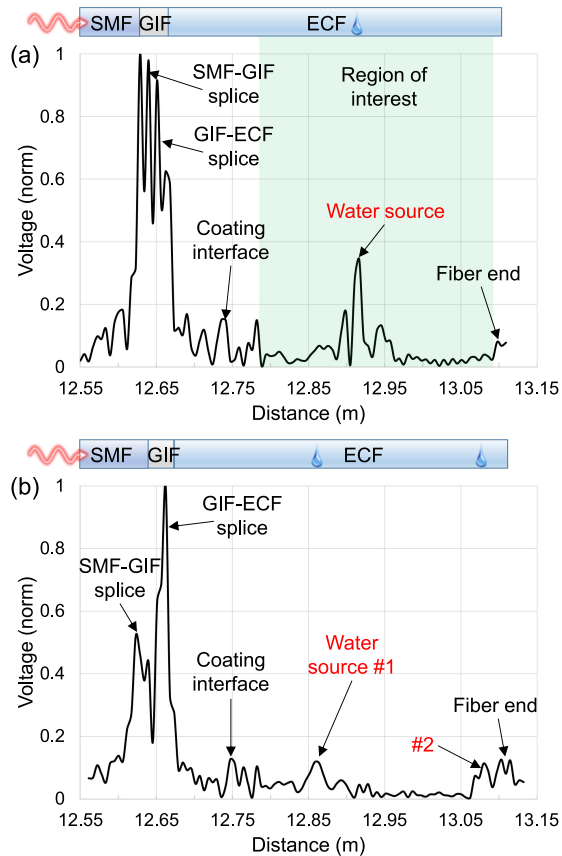
Fig. 6. Spatially resolved measurement data of a sensing fiber with a 10.0 bilayer PEM coating, involving: (a) a single water source; and (b) two water sources. Voltages are normalized by the highest peak of the dual-splice fiber region. Exposed-core fiber: ECF, graded-index fiber: GIF, and single-mode fiber: SMF.

3.4–62.3 pW). To increase the sensitivity, a high-order mode and/or more RI-responsive functional coating material could be used. Temperature tests on the sensing fibers indicated a weak cross-sensitivity.

VII. SPATIAL CHARACTERIZATION

To test the spatial-resolving performance of the distributed water sensor, a wet tissue was used to transfer water to a specific position along the metal-pipe-bound sensing fiber with a 10.0 bilayer PEM coating. The optical response is shown in Figure 6(a). The C-OFDR identified reflections from the two fiber splices, the PEM coating edge, the water source at a distance of 12.92 m, and the sensing fiber termination. The reflection of the dual-splice fiber region is relatively high, and it is attributed to the much higher transmitted-power at the start of the sensing fiber. Similarly, Figure 6(b) shows the positions of two water sources, at 12.86 m and 13.07 m. The side peaks are not artefacts but stray water contacts. There is no distinction between lower or higher peaks above the noise floor along the sensing fiber, as they all denote water sources. The peak amplitude differences are mainly attributed to the different angles of water-coating interface and the volume of water. The variation in the shape (i.e., splice dependent), width and amplitude of back-reflected peaks are associated with ambient temperature drifts influencing the
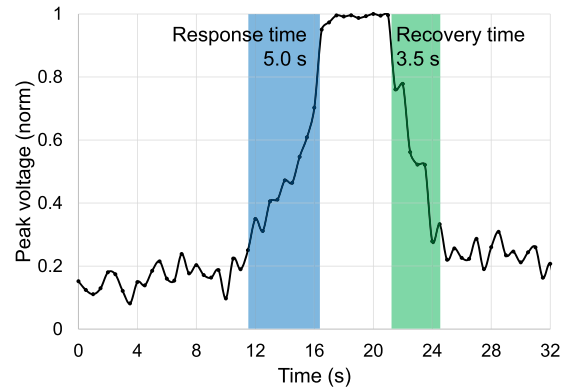

Fig. 7. Temporally resolved measurement data of the sensing fiber with a 10.0 bilayer PEM coating, involving a single water source. Peak voltages are normalized by the highest peak within the displayed time range.

state of polarization, which affects the reflectivity of packaged splice points. Similar results were obtained with sensing fibers with 6.0, 8.0, 12.0 and 14.0 bilayer PEM coatings.

The observed spatial resolution shown in Figure 6 in terms of the beat frequency width is in good agreement with the calculated Δz of 4.6 mm (i.e., see detection system setup section). This is the smallest spatial resolution demonstrated for distributed sensors employing ECF. An earlier work based on fully distributed fluorescence-based sensing employed ECF of 20 cm length [30]. Owing to fluorescence-life-time- and modal-dispersion-induced pulse broadening (i.e., heavily multimode), Δz of ∼5 m can be inferred from the pulse width in their results [30].

Owing to the effective RI difference between the sensing and reference fibers, the distance scale was adjusted based on the effective-RI ratio. For example, the effective RI of the sensing and reference fibers are 1.35 (i.e., ambient state with coating) and 1.444 respectively, from COMSOL modeling. This requires the distance scale for the coated fiber section to be multiplied by a factor of $1.444/1.35 = 1.07$. Furthermore, water-induced changes in the RI introduce phase delays along the sensing fiber, which can decrease its optical path length, and thus minor distance errors accumulate for water sources beyond the first position.

VIII. TEMPORAL CHARACTERIZATION

To test the temporal characteristics of the distributed water sensor, a wet tissue was again used to perturb the metal-pipe-bound sensing fiber with a 10.0 bilayer PEM coating at an arbitrary position, and the water-induced peak voltage was monitored as a function of time. The standard approach to suppress equilibrium-ambiguity was adopted by taking the temporal characteristics between 10–90% of the maximum voltage. Figure 7 shows the peak voltage slowly rising with water absorption from the attachment of the wet tissue (i.e., response time), before the wet tissue was detached from the sensing fiber, where the peak voltage gradually dropped back to its neutral level (i.e., recovery time). The recovery time of 3.4 s was slightly shorter than the response time of 4.8 s, because generally water flows to the core of the sensing fiber in a slower and non-uniform manner, while water evaporates from the core via ambient airflow at

a faster and more uniform way. Generally, the response time ranges between 4–6 s and recovery time ranges between 3–5 s.

Temporal results obtained from the sensing fibers with 6.0, 8.0, 12.0 and 14.0 bilayer PEM coatings revealed response times ranging between 3–5 s, 4–6 s, 5–7 s and 5–7 s respectively, and recovery times ranging between 2–4 s, 3–5 s, 4–6 s and 4–6 s respectively. This was anticipated because thinner PEM coatings can enable faster water propagation, and thus reach dry and wet equilibrium states more quickly [18]. The response time of the distributed humidity sensor based on the 10.0 bilayer PEM coating was measured to be significantly shorter between 1–2 s, while the recovery time remained similar between 3–5 s. The reason behind this faster response lies with the faster propagation of water vapor compared to water through the ECF trench. One way to quicken the temporal characteristics is to make the trench of the ECF shallower, such that water can enter and escape faster. However, this will make fiber splicing more challenging due to the increased offset of the fiber core.

IX. Discussions

In Figure 4(b), RH ambiguity arises on either side of the ambient condition of 45%RH due to the nature of distributed reflectometry techniques being suited to undertake relative RI-based measurements between fiber segments along the sensing fiber. As a result, positive or negative RI changes between adjacent coating segments generate the same reflectivity. For this lab demonstration, all the RI changes are adjacent and relative to the ambient RI, such that there are no cases where two adjacent segments of the sensing fiber exhibit non-ambient RI. Although cross-correlation processing of the frequency-domain spectrum of the Rayleigh back-scattered light can usually provide absolute measurements, it cannot function with the evanescent-field-based sensing mechanism that simultaneously changes both amplitude (i.e., from external effects) and frequency shift (i.e., from Rayleigh back-scattering and external effects). Another issue that could occur in a real measurement environment is gradual changes in RH along the sensing fiber that can lead to low reflectivity and thus weak back-reflected signals.

Both of these problems could be solved if we isolate the sensing fiber from the local RH in at periodic intervals to facilitate sharp referenced RH contrasts between exposures to the local RH for taking absolute RH measurements with high sensitivity. This is possible with periodic ultra-short segments of PEM coatings and waterproof coating in-between, which exhibits the same RI as the PEM coating at 0%RH or 100%RH, and not the RI corresponding to the ambient RH. Although the periodic-coating approach offers an inexpensive way to vastly extend the sensing range and sensitivity, the resulting sensor becomes a low-range high spatial-resolution quasi-distributed humidity sensor. For practical application, the sensing fiber can be inserted into a protective tube containing "breathing" holes that serves to shield the sensing fiber from unwanted external effects, while retaining access to the local RH.

As with distributed reflectometry techniques, perturbations at positions closer to the start of the sensing fiber affect subsequent position determination along the sensing fiber. Hence, to provide an accurate measure of multiple sources of water vapor, the amplitude of each back-reflected peak must be rescaled as a function of reflectivity and propagation loss related to the previously detected peaks. Such complex signal processing is beyond the scope of this work, and will be simpler to address in future work with the quasi-distributed design. This is because of the unpredictable distribution of water molecules (i.e., continuous coating rather than ultra-short segments) within the spatial resolution (i.e., reflectivity might not always be proportional to RH).

Although only ∼35 cm of sensing fiber was tested due to the limitation of the coating rig, it can be up to ∼50 cm with the existing sensing fiber (i.e., see detection system setup section). This sensing range can find uses in measuring water or RH at different depths. If the propagation loss of the sensing fiber can be reduced (e.g., use a non-water-absorbing wavelength [28] and/or a coating material with a smoother surface), longer sensing ranges are possible. An alternative solution is to use multiplex an array of short-range sensing fibers with an optical switch, such that each sensing fiber is deployed at a different depth, with low-loss standard optical fibers for connections. Simultaneous monitoring of water or RH is possible by rapidly switching between the different channels connected to different sensing fibers.

X. Conclusions

We have made significant progress in distributed sensing with the first short-range demonstrations towards non-bending distributed water and humidity sensors based on an exposed-core fiber with a low-cost polyelectrolyte multilayer coating interrogated using coherent optical frequency-domain reflectometry. This new sensing platform is enabled by the first combination of small-core exposed-core fiber, functional coating, and coherent optical frequency-domain reflectometry, which could pave the way to a multitude of fully distributed bio/chemical sensors. The sensing fiber can be configured between being sensitive to only water (i.e., 6.0, 8.0, 14.0 bilayer coatings), or both water and water vapor (i.e., 10.0, 12.0 bilayer coatings), by choosing precise coating thicknesses. The demonstrated average sensitivity of the sensing fiber with 10.0 bilayer polyelectrolyte multilayer coating to relative humidity via refractive-index change varies from 0.060–0.001/%RH (0–38 cm distance) within a dynamic range of 26–95%RH. The distance-dependent detection limit varies between 0.3–10.0%RH (0–38 cm distance), and the spatial resolution of 4.6 mm is the smallest demonstrated for exposed-core fibers and can be vastly improved by simply broadening the swept range. A short-range demonstration yields a sensing range of ∼0.5 m, which is more suitable for water-depth monitoring than distributed humidity sensing. It can be extended by lowering the propagation loss with a non-water-absorbing wavelength. The response and recovery times are 4–6 s and 3–5 s respectively for 10.0 bilayers. The existing sensor (i.e., fully distributed) is a solution for water-depth monitoring, and an intermediate solution for distributed humidity sensing. For the latter, it is limited in terms of RH ambiguity on either side of the ambient RH; unable to quantify multiple

distance-dependent signals; and short-range operation. Future work (i.e., quasi-distributed) based on segmented ultra-short sections of PEM coating is anticipated to solve these issues, by providing sharp referenced RI sections with short propagation lengths under water-induced absorption loss.

APPENDIX

A. Sensing Fiber Coating

Prior to coating the exposed region of the ECF, the ECF was cleaned and hydroxylated via immersion in piranha solution (1:3 (v/v) mixture of 30% H_2O_2 and 98% H_2SO_4) for 1 hr, followed by rinsing with deionized water several times. After this treatment, alternating immersion of the ECF into the aqueous solutions of PDDA (1 mg/mL) then PSS (1 mg/mL) was carried out in the presence of NaCl (1.0 M) for 20 min until the desired layer number was achieved with PSS as the outmost layer. Each immersion step was followed by rigorous rinsing with deionized water ($>$18.2 MΩ cm^{-1}) and dried with N_2 gas.

REFERENCES

[1] T. A. Ghebreyesus and A. Lake, "Progress on drinking water, sanitation and hygiene: 2017 update and SDG baselines," *World Health Organization*, 2017. [Online]. Available: http://apps.who.int/iris/bitstream/10665/258617/1/9789241512893-eng.pdf?ua = 1

[2] J. M. Corres, F. J. Arregui, and I. R. Matias, "Design of humidity sensors based on tapered optical fibers," *J. Lightw. Technol.*, vol. 24, no. 11, pp. 4329–4336, Nov. 2006.

[3] A. Kharaz and B. E. Jones, "A distributed optical-fibre sensing system for multi-point humidity measurement," *Sens. Actuators A*, vol. 47, no. 1–3, pp. 491–493, Mar./Apr. 1995.

[4] L. Schenato, "A review of distributed fibre optic sensors for geo-hydrological applications," *Appl. Sci.*, vol. 7, no. 896, pp. 1–42, Sep. 2017.

[5] C. A. Galindez-Jamioy and J. M. López-Higuera, "Brillouin distributed fiber sensors: An overview and applications," *J. Sens.*, vol. 6, Aug. 2012, Art. no. 204121.

[6] M. Ramakrishnan, G. Rajan, Y. Semenova, and G. Farrell, "Overview of fiber optic sensor technologies for strain/temperature sensing applications in composite materials," *Sensors*, vol. 16, no. 1, Jan. 2016, Art. no. 99.

[7] A. Rogers, "Distributed optical-fibre sensors for the measurement of pressure, strain and temperature," *Phys. Rep.*, vol. 169, no. 2, pp. 99–142, Oct. 1988.

[8] T. P. Newson and A. Masoudi, "Analysis of distributed optical fibre acoustic sensors through numerical modelling," *Opt. Express*, vol. 25, no. 25, pp. 32021–32040, Dec. 2017.

[9] A. Stefani, S. Andresen, W. Yuan, N. Herholdt-Rasmussen, and O. Bang, "High sensitivity polymer optical fiber-Bragg-grating based accelerometer," *IEEE Photon. Technol. Lett.*, vol. 24, no. 9, pp. 763–765, May 2012.

[10] S. Srivastava, S. Rao D. S., and H. Nandakumar, "Novel optical gyroscope: Proof of principle demonstration and future scope," *Sci. Rep.*, vol. 6, Oct. 2016, Art. no. 34634.

[11] Z. Tian and S. S. H. Yam, "In-line single-mode optical fiber interferometric refractive index sensors," *J. Lightw. Technol.*, vol. 27, no. 13, pp. 2296–2306, Jul. 2009.

[12] P. Wang, Y. Wang, and L. Tong, "Functionalized polymer nanofibers: A versatile platform for manipulating light at the nanoscale," *Lightw. Sci. Appl.*, vol. 2, Oct. 2013, Art. no. e102.

[13] G. Y. Chen, X. Wu, X. Liu, D. G. Lancaster, T. M. Monro, and H. Xu, "Photodetector based on vernier-enhanced fabry-perot interferometers with a photo-thermal coating," *Sci. Rep.*, vol. 7, 2017, Art. no. 41895.

[14] W. C. Michie *et al*., "Distributed sensor for water and pH measurements using fiber optics and swellable polymeric systems," *Opt. Lett.*, vol. 20, no. 1, pp. 103–105, Jan. 1995.

[15] H. Shi *et al*., "Automated online optical biosensing system for continuous real-time determination of microcystin-LR with high sensitivity and specificity: Early warning for cyanotoxin risk in drinking water sources," *Environ. Sci. Technol.*, vol. 47, no. 9, pp. 4434–4441, May 2013.

[16] E. P. Schartner *et al*., "Taming the light in microstructured optical fibers for sensing," *Int. J. Appl. Glass Sci.*, vol. 6, no. 3, pp. 229–239, Jul. 2015.

[17] L. Yu *et al*., "Ultrafast colorimetric humidity-sensitive polyelectrolyte coating for touchless control," *Mater. Horiz.*, vol. 4, no. 1, pp. 72–82, Jan. 2017.

[18] G. Y. Chen *et al*., "Ultra-fast hygrometer based on U-shaped optical microfiber with nanoporous polyelectrolyte coating," *Sci. Rep.*, vol. 7, Aug. 2017, Art. no. 7943.

[19] H. Y. Fu, H. L. Liu, W. H. Chung, and H. Y. Tam, "A novel fiber Bragg grating sensor configuration for long-distance quasi-distributed measurement," *IEEE Sens. J.*, vol. 8, no. 9, pp. 1598–1602, Aug. 2008.

[20] B. J. Soller, D. K. Gifford, M. S. Wolfe, and M. E. Froggatt, "High resolution optical frequency domain reflectometry for characterization of components and assemblies," *IEEE Photon. J.*, vol. 13, no. 2, pp. 666–674, Jan. 2005.

[21] J. Song, W. Li, P. Lu, Y. Xu, L. Chen, and X. Bao, "Long-range high spatial resolution distributed temperature and strain sensing based on optical frequency-domain reflectometry," *IEEE Photon. J.*, vol. 6, no. 3, Apr. 2014, Art. no. 6801408.

[22] E. P. Schartner, A. Dowler, and H. Ebendorff-Heidepriem, "Fabrication of low-loss, small-core exposed core microstructured optical fibers," *Opt. Mater. Express*, vol. 7, no. 5, pp. 1496–1502, May 2017.

[23] G. Y. Chen, M. Ding, T. P. Newson, and G. Brambilla, "A review of microfiber and nanofiber based optical sensors," *Open Opt. J.*, vol. 7, pp. 32–57, Dec. 2013.

[24] H. Ebendorff-Heidepriem, S. C. Warren-Smith, and T. M. Monro, "Suspended nanowires: Fabrication, design and characterization of fibers with nanoscale cores," *Opt. Express*, vol. 17, no. 4, pp. 2646–2657, Feb. 2009.

[25] A. Toutianoush, L. Krasemann, and B. Tieke, "Polyelectrolyte multilayer membranes for pervaporation separation of alcohol/water mixtures," *Colloids Surf. A*, vol. 198-200, pp. 881–889, Feb. 2002.

[26] D. B. Asay and S. H. Kim, "Evolution of the adsorbed water layer structure on silicon oxide at room temperature," *J. Phys. Chem. B.*, vol. 109, no. 35, pp. 16760–16763, Sep. 2005.

[27] M. N. Polyanskiy, "Optical constants of SiO2. Refractive index database," *Refractive Index Database*, 2018. [Online]. Available: https://refractiveindex.info/?shelf = main&book = SiO2&page = Malitson

[28] D. K. Srivastava, M. Weinrotter, H. Kofler, A. K. Agarwal, and E. Wintner, "Laser-assisted homogeneous charge ignition in a constant volume combustion chamber," *Opt. Lasers Eng.*, vol. 47, no. 6, pp. 680–685, Jun. 2009.

[29] N. Riesen, T. Lam, and J. H. Chow, "Resolving the range ambiguity in OFDR using digital signal processing," *Meas. Sci. Technol.*, vol. 25, Oct. 2014, Art. no. 125102.

[30] R. Kostecki, H. Ebendorff-Heidepriem, C. Davis, G. McAdam, T. Wang, and T. M. Monro, "Fiber optic approach for detecting corrosion," *Proc. SPIE.*, vol. 9803, Apr. 2016, Art. no. 98031I.

Authors' biographies not available at the time of publication.